GDCh

Research Article

Angewandte
Chemie
International Edition
www.angewandte.org

Check for updates

Solid-state Electrolytes

Tuning Ion Mobility in Lithium Argyrodite Solid Electrolytes via Entropy Engineering

Jing Lin, Mareen Schaller, Sylvio Indris, Volodymyr Baran, Ajay Gautam, Jürgen Janek, Aleksandr Kondrakov, Torsten Brezesinski,* and Florian Strauss*

Abstract: The development of improved solid electrolytes (SEs) plays a crucial role in the advancement of bulk-type solid-state battery (SSB) technologies. In recent years, multicomponent or high-entropy SEs are gaining increased attention for their advantageous charge-transport and (electro)chemical properties. However, a comprehensive understanding of how configurational entropy affects ionic conductivity is largely lacking. Herein we investigate a series of multication-substituted lithium argyrodites with the general formula $Li_{6+x}[M1_aM2_bM3_cM4_d]S_5I$, with M being P, Si, Ge, and Sb. Structure-property relationships related to ion mobility are probed using a combination of diffraction techniques, solid-state nuclear magnetic resonance spectroscopy, and charge-transport measurements. We present, to the best of our knowledge, the first experimental evidence of a direct correlation between occupational disorder in the cationic host lattice and lithium transport. By controlling the configurational entropy through compositional design, high bulk ionic conductivities up to 18 mS cm^{-1} at room temperature are achieved for optimized lithium argyrodites. Our results indicate the possibility of improving ionic conductivity in ceramic ion conductors via entropy engineering, overcoming compositional limitations for the design of advanced electrolytes and opening up new avenues in the field.

Introduction

With the growing demand for mature electrochemical energy-storage devices, solid-state batteries (SSBs) have emerged as a promising technology due to their high (practical) energy and powder densities and improved safety. Ion conductors with superionic conductivity, good (electro)chemical stability, and easy processability are key enablers for such technology.[1,2] Currently, different material classes such as sulfides, halides, hydrides, and oxides are under investigation, with each of them having advantages and disadvantages.[2,3] Among them, lithium thiophosphates, including $Li_{10}GeP_2S_{12}$, $Li_2S-P_2S_5$ glasses, and argyrodite Li_6PS_5X (X=Cl, Br, I), have attracted considerable attention owing to high room-temperature ionic conductivities, which are comparable to those of liquid electrolytes, along with mechanical softness.[3,4]

Lithium argyrodites are built up from $[PS_4]^{3-}$ tetrahedral units, free X$^-$ and S^{2-} ions forming a cubic crystal skeleton, and Li$^+$ being located on different partially occupied crystallographic sites, thereby offering a framework for fast ion diffusion.[5,6] Starting from the initially reported, poorly conducting lithium argyrodite Li_6PS_5I, the conductivity could be significantly improved via substitution on the phosphorus site. For example, high ionic conductivities have been reported for $Li_{6.6}P_{0.4}Ge_{0.6}S_5I$ (5.4 mS cm^{-1}, cold-pressed state) or $Li_{6.7}Si_{0.7}Sb_{0.3}S_5I$ (12.6 mS cm^{-1}, cold-pressed state) and rationalized by facilitated lithium diffusion enabled by increased S^{2-}/I$^-$ site inversion and/or occupation of additional lithium positions and therefore shortened Li–Li intercage jump distances.[7,8] Achieving high ionic conductivity in argyrodites depends on various parameters such as balanc-

---

[*] J. Lin, J. Janek, A. Kondrakov, T. Brezesinski, F. Strauss
Battery and Electrochemistry Laboratory (BELLA), Institute of Nanotechnology (INT), Karlsruhe Institute of Technology (KIT), Hermann-von-Helmholtz-Platz 1, 76344 Eggenstein-Leopoldshafen, Germany
E-mail: torsten.brezesinski@kit.edu
        florian.strauss@kit.edu

M. Schaller, S. Indris
Institute for Applied Materials—Energy Storage Systems (IAM-ESS), Karlsruhe Institute of Technology (KIT), Hermann-von-Helmholtz-Platz 1, 76344 Eggenstein-Leopoldshafen, Germany

V. Baran
Deutsches Elektronen-Synchrotron DESY, Notkestr. 85, 22607 Hamburg, Germany

A. Gautam
Section Storage of Electrochemical Energy, Radiation Science and Technology, Faculty of Applied Sciences, Delft University of Technology, Delft 2629 JB, The Netherlands

J. Janek
Institute of Physical Chemistry & Center for Materials Research (ZfM/LaMa), Justus-Liebig-University Giessen, Heinrich-Buff-Ring 17, 35392 Giessen, Germany

A. Kondrakov
BASF SE, Carl-Bosch-Str. 38, 67056 Ludwigshafen, Germany

---

ing the density of charge carriers and vacancies, altering the polyhedral volume, and introducing site disorder.[4] These factors can broaden the lithium diffusion pathways and shorten the jump distances between the cages, thus positively affecting ion diffusion.[9–11] All of these parameters can be tailored in a given (argyrodite) crystal structure via iso- or aliovalent substitution in the host lattice.[4,12]

Deviating from this rather classical strategy, multielement-substituted (high-entropy) solid electrolytes (SEs) have recently attracted much attention. Such materials are capable of overcoming compositional limitations, which in turn may help to accelerate the development of advanced SEs.[13] Aside from that, high-entropy SEs allow for the possibility of a flattened energy landscape for ion transport through strong (local) lattice distortions.[14–16] The term "high entropy" commonly refers to materials with a configurational entropy of $\Delta S_{\mathrm{conf}} \geq 1.5R$, with R representing the gas constant, which can be calculated from shared occupancies over similar crystallographic sites.[13,17] In general, systematic control over ΔS_{conf} through compositional variations, i.e. entropy engineering, has rarely been achieved. Furthermore, the solubility of dopants/substituents in materials can potentially be increased to such an extent that the optimum charge-carrier concentration is achieved and/or improved properties emerge.

With regards to compositionally complex SEs, only a few materials have been reported up until now, including garnet, perovskite, Na SuperIonic CONductor (NASICON), halide, argyrodite, and $Li_{10}GeP_2S_{12}$ (LGPS)-type samples.[15,16,18–26] For high-entropy LGPS-type $(Li_{9.54}[Si_{0.6}Ge_{0.4}]_{1.74}P_{1.44}S_{11.1}Br_{0.3}O_{0.6})$ and lithium argyrodite materials (e.g. $Li_{6.5}[P_{0.25}Si_{0.25}Sb_{0.25}Ge_{0.25}]S_5I$ and $Li_{5.5}PS_{4.5}Cl_{0.8}Br_{0.7}$), high ionic conductivities (>10 mS cm^{-1} at room temperature) could be realized in practice.[15,16,21,23] To unlock the potential of high-entropy ion conductors for SSB application, a detailed understanding of the role of configurational entropy on charge transport, as well as on the (electro)chemical and mechanical properties is required. However, direct correlation between the degree of disorder and the ionic conductivity remains elusive because of the challenge in separating configurational entropy from other effects. Nevertheless, Li et al. have recently reported on the relationship between compositional disorder in the anion sublattice and ionic conductivity of $Li_{5.5}PS_{4.5}Cl_xBr_{1.5-x}$ solid solutions.[23] However, the effect of occupational disorder (configurational entropy) induced by multicationic substitution in lithium argyrodites has not been investigated yet.

In the present work, we attempt to disentangle the effect of configurational entropy on ion mobility in Li_{6+x}-$[M1_aM2_bM3_cM4_d]S_5I$ (M=P, Si, Ge, and Sb) from other structural parameters. A series of samples were successfully synthesized and their crystal structure examined through synchrotron X-ray diffraction (SXRD), neutron powder diffraction (NPD), and ^{31}P, ^{29}Si, and ^{6}Li magic-angle spinning (MAS) nuclear magnetic resonance (NMR) spectroscopy measurements. The charge-transport properties were probed using complementary electrochemical impedance spectroscopy (EIS) and ^{7}Li pulsed-field gradient (PFG) NMR spectroscopy. It is shown that structural (occupational) disorder strongly increases the Li-ion conductivity and lowers the energy barrier for diffusion.

Results and Discussion

A series of multication-substituted lithium argyrodites were prepared by high-energy ball milling and post-annealing at 500 °C in vacuum-sealed quartz ampules (see Supporting Information for details). The respective samples are referred to as P$_{0.75}$, P$_{0.5}$, Si$_{0.5}$, EQ, Ge$_{0.5}$, Sb$_{0.5}$, and Sb$_{0.75}$ hereafter (Table 1). Other compositions, which have been synthetically explored but did not yield single-phase materials are reported elsewhere.[15] Structural characterization using laboratory XRD revealed reflections consistent with the cubic argyrodite structure, and the patterns showed a gradual shift in the position of the reflections (Figure S1, Supporting Information). The chemical composition of the samples was studied by inductively coupled plasma-optical emission spectroscopy (ICP-OES), confirming the targeted stoichiometries (Table S1, Supporting Information).

To examine the crystal structure, SXRD and NPD measurements were conducted on the different materials. The room-temperature SXRD and NPD patterns for $Li_{6.66}[P_{0.167}Si_{0.5}Ge_{0.167}Sb_{0.167}]S_5I$ (Si$_{0.5}$), as well as the corresponding Rietveld refinement profiles are shown in Figure 1a and b, respectively. The patterns can be indexed in the *F*-43*m* space group, with lattice parameter $a =$ 10.28599(1) Å and 10.2867(3) Å and cell volume $V =$ 1088.274(2) Å^3 and 1088.51(9) Å^3, respectively. Structural parameters from refinements for all samples are given in Tables S2–S14 (Supporting Information). Notably, the lattice parameters derived from SXRD and NPD are in excellent agreement with one another (Figure S2, Supporting Information). As expected, the observed increase in lattice parameter upon substituting Si^{4+}, Ge^{4+}, and Sb^{5+} for P^{5+} is consistent with variations in ionic radii and stoichiometries, thus confirming successful multicationic substitution.[27] The calculated crystal structure for Si$_{0.5}$ is shown in Figure 1c. Both the S^{2-} and I$^-$ ions form a face-centered cubic sublattice (Wyckoff position 4a). Additionally, the S^{2-} and I$^-$ ions also occupy half of the tetrahedral voids (Wyckoff position 4d). The rest of the S^{2-} ions resides on the Wyckoff position 16e around the octahedral sites (central atom on Wyckoff position 4b), forming $[P_{0.167}Si_{0.5}Ge_{0.167}Sb_{0.167}S_4]^{3.66-}$ tetrahedra, which can be consid-

Table 1: The multication-substituted argyrodite SEs prepared and characterized in this work.

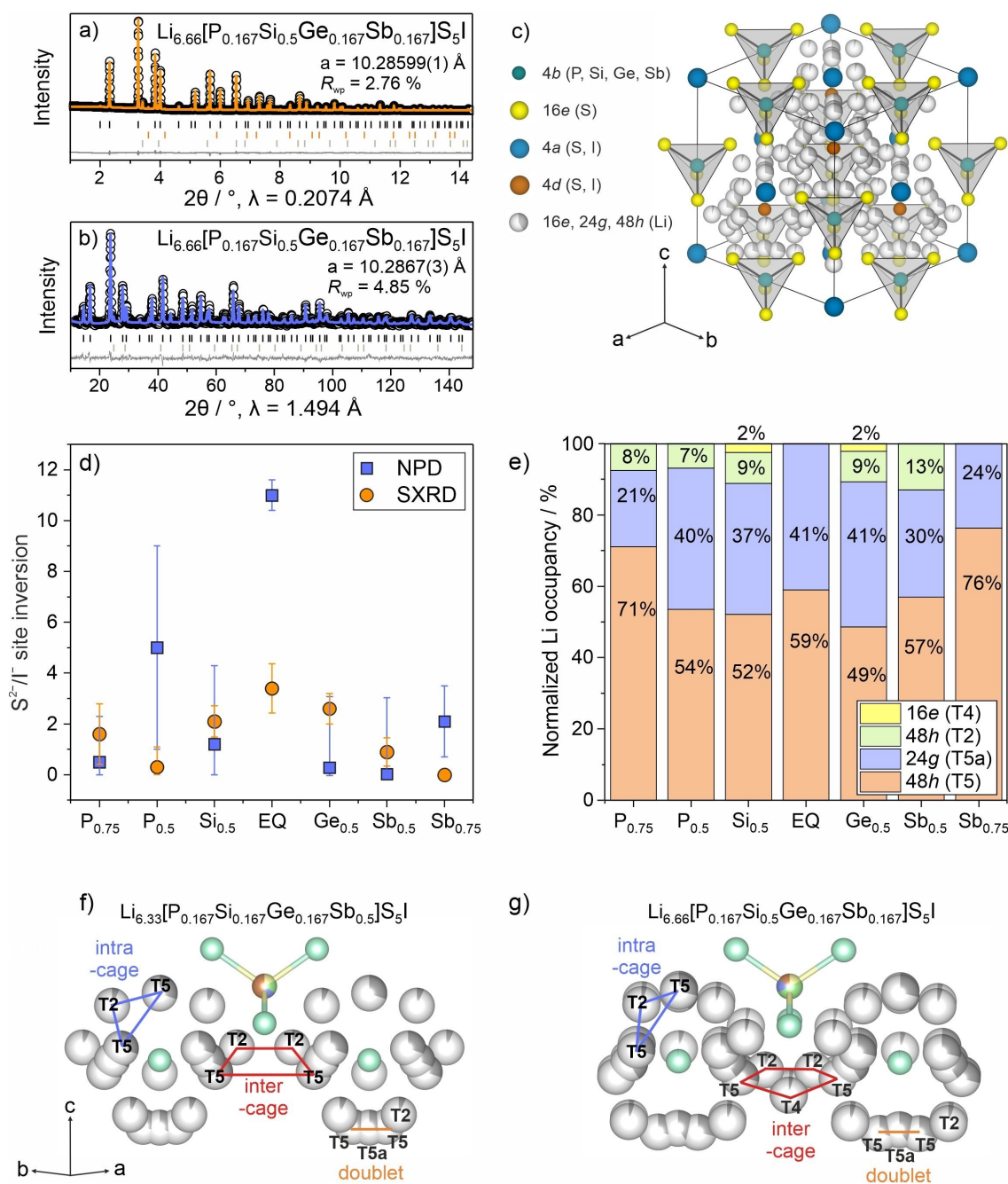| Label	Nominal composition
P$_{0.75}$	$Li_{6.17}[\mathbf{P_{0.75}}Si_{0.083}Ge_{0.083}Sb_{0.083}]S_5I$
P$_{0.5}$	$Li_{6.33}[\mathbf{P_{0.5}}Si_{0.167}Ge_{0.167}Sb_{0.167}]S_5I$
Si$_{0.5}$	$Li_{6.66}[P_{0.167}\mathbf{Si_{0.5}}Ge_{0.167}Sb_{0.167}]S_5I$
Equimolar (EQ)	$Li_{6.5}[P_{0.25}Sb_{0.25}Si_{0.25}Ge_{0.25}]S_5I$
Ge$_{0.5}$	$Li_{6.66}[P_{0.167}Si_{0.167}\mathbf{Ge_{0.5}}Sb_{0.167}]S_5I$
Sb$_{0.5}$	$Li_{6.33}[P_{0.167}Si_{0.167}Ge_{0.167}\mathbf{Sb_{0.5}}]S_5I$
Sb$_{0.75}$	$Li_{6.17}[P_{0.083}Si_{0.083}Ge_{0.083}\mathbf{Sb_{0.75}}]S_5I$

Figure 1. Structural characterization of the multication-substituted argyrodite SEs. (a) SXRD and (b) NPD patterns of $Li_{6.66}[P_{0.167}Si_{0.5}Ge_{0.167}Sb_{0.167}]S_5I$ ($Si_{0.5}$) with corresponding Rietveld refinement profiles. Black circles are the experimental data, orange (SXRD) and blue (NPD) lines the calculated patterns, and gray lines represent the difference profiles. Vertical tick marks denote the position of expected Bragg reflections [black (argyrodite), light gray (LiI), yellow (Li_2S)]. (c) Schematic illustration of the crystal structure for $Si_{0.5}$ with Wyckoff positions and elemental constituents indicated in the legend to the left. (d) Anion site inversion determined by Rietveld analysis of SXRD (orange) and NPD (blue) data. (e) Normalized Li occupancies. (f,g) Schematic illustrations of two neighboring Li cages. The data for EQ in (d) and (e) was taken from the literature.[15,21] If error bars are not visible, the standard deviation is smaller than the data symbol.

ered as a combination of $[PS_4]^{3-}$, $[SiS_4]^{4-}$, $[GeS_4]^{4-}$, and $[SbS_4]^{3-}$. In the argyrodite structure, S^{2-} ($4d$) and I^- ($4a$) are known to mix over the respective Wyckoff positions, referring to anion site inversion (through aliovalent substitution on the phosphorus site).[8,28] Rietveld analysis of the SXRD and NPD data allowed for quantification of the degree of site inversion, as shown in Figure 1d. The differ-

ences between the site inversion determined by SXRD and NPD lie in the standard deviation range, except for $Li_{6.5}[P_{0.25}Si_{0.25}Ge_{0.25}Sb_{0.25}]S_5I$ (EQ). Note that site inversion also depends upon the Li substructure (surrounding the $4d$ Wyckoff position) and the tetrahedral environment,[4] and therefore the large discrepancy seen for EQ could be a result of its intrinsic complexity.

Rietveld analysis of NPD data further offered insights into the structural arrangement of the Li sublattice. Figure 1e depicts the normalized Li occupancies over the different crystallographic sites. As can be seen, lithium predominantly occupies type (T) 5 ($48h$) and 5a ($24g$) Wyckoff sites in all samples. However, in the case of $P_{0.75}$, $P_{0.5}$, $Si_{0.5}$, $Ge_{0.5}$, and $Sb_{0.5}$, a fraction of type 2 ($48h$) Wyckoff sites was also occupied. Moreover, for the primarily aliovalent substituted lithium argyrodites, such as $Si_{0.5}$ and $Ge_{0.5}$, additional occupancy was found for type 4 ($16e$) Wyckoff sites, with relatively low occupation values of about $(2\pm0.1)\%$, see Figure 1e. It is worth noting that for EQ, only two Li positions were identified. This could be associated with the highly distorted tetrahedral environment, where both type 2 and 4 may be considered metastable and thus difficult to detect. In turn, this also leads to the challenge of precisely determining anion disorder, as the Li sublattice and site inversion are closely related, which helps explain the deviation in S^{2-}/I^- between SXRD and NPD, with similar observations made for $Li_{6.5}P_{0.5}Ge_{0.5}S_5I$.[29] To illustrate the diffusion pathways, the Li substructure is shown in Figures 1f,g, and S3 (Supporting Information). Three different jumps were identified for the materials contributing to long-range 3D lithium diffusion, namely $48h$(T5)-$48h$(T5) doublet jumps [through the nominal $24g$(T5a) transition site], intracage jumps between two adjacent $48h$(T5) tetrahedra, and intercage jumps between $48h$(T5) positions. Lithium argyrodites in which the Li^+ ions only occupy the $48h$(T5) and $24g$(T5a) Wyckoff sites usually have poor transport properties, due to long intercage jump distances.[4,29,30] In a previous study, we have demonstrated that EQ possesses a shortened intercage jump distance, thereby facilitating ion mobility.[15] This jump distance is also shorter compared to $Sb_{0.75}$, thus rationalizing the fast diffusion kinetics for EQ. With T2($48h$) being occupied (Figure 1e), connections between T5 sites within the same Li cage are established, leading to fast intracage motion via T5-T2-T5 pathways (blue lines in Figure 1f,g). More importantly, T2 serves as an "intermediate" position bridging two T5 sites from different cages, enabling intercage jumping via T5-T2-T2-T5 pathways with much shortened distances (red lines in Figure 1f,g). Typically, the T5-T2 and T2-T2 distances are much shorter than that of isolated T5-T5 jumping. Additionally occupied T4 sites further promote long-range diffusion (low energy barrier) by connecting different Li cages through T5-T4-T5 pathways. The Li–Li jump distances for the different samples are given in Table S15 (Supporting Information).

In summary, multicationic substitution in lithium argyrodites strongly affects the Li sublattice and favors ion diffusion through shortened Li–Li jump distances, in some cases by occupation of additional crystallographic sites. However, it should be noted that the appearance of additionally occupied sites (T2 and T4) is presumably also connected, at least to some degree, to the overall Li content.

To investigate the local environment surrounding phosphorus and silicon, ^{31}P and ^{29}Si MAS NMR spectroscopy measurements were performed (Figure 2a,b). All samples exhibit a distinct ^{31}P peak between 90 and 96 ppm
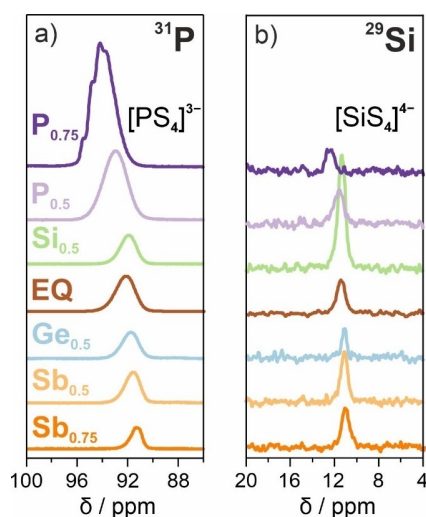

Figure 2. (a) ^{31}P and (b) ^{29}Si MAS NMR spectra collected from the multication-substituted argyrodite SEs. The data for EQ was taken from the literature.[15,21]

characteristic of the $[PS_4]^{3-}$ tetrahedral environment. This is consistent with previous observations on other lithium thiophosphate SEs.[5,14,15,21,23,31,32] The ^{31}P intensity decreased from $P_{0.75}$ to $Sb_{0.75}$, with the peak gradually shifting from 94.05 to 91.3 ppm (Figure S4, Supporting Information). In the case of $P_{0.75}$, the spectrum also revealed several contributions indicated by shoulder peaks at higher ppm values. Multiple contributions in the ^{31}P spectrum are often associated with the S^{2-}/X^- site inversion (X=Cl^-, Br^-, I^-) in lithium argyrodites.[5,14,23,32] However, considering the low degree of S^{2-}/I^- (1.19% from SXRD and 0.5% from NPD), the latter can be ruled out for $P_{0.75}$. This suggests that it is potentially determined by other structural distortions, which strongly depend on the local arrangement of neighboring tetrahedral species (i.e. $[SiS_4]^{4-}$, $[GeS_4]^{4-}$, and $[SbS_4]^{3-}$). The ^{29}Si spectra also showed a single contribution at ~11 ppm for all samples, with no obvious trend in peak shift with varying composition. However, both the appearance of a single peak and the chemical shift confirm the $[SiS_4]^{4-}$ tetrahedral environment and corroborate the absence of impurity phases.[15,21,33–35]

Additionally, ^6Li MAS NMR spectra were recorded, revealing a narrow peak located around 1.2 ppm, which is indicative of fast Li motion (Figure S5, Supporting Information).[15,21,23,29,31] Overall, similar spectra with no apparent signs of impurity contributions were obtained for the multication-substituted SEs, confirming the robustness of the argyrodite lattice.

After characterizing the long-range and local structural features of the samples, the charge-transport properties were examined via EIS and ^7Li PFG NMR spectroscopy. EIS measurements were conducted on sintered pellets in the temperature range of 15–65°C (Figure S6, Supporting Information). Fitting of the spectra revealed room-temperature ionic conductivities ranging from (0.043 ± 0.004) mS cm^{-1} for $P_{0.75}$ to (14.05 ± 1.019) mS cm^{-1} for $Ge_{0.5}$. The fitting results are given in Table S16 (Supporting

Information), indicating that for EQ, $Si_{0.5}$, and $Ge_{0.5}$, ionic conductivities above $12\ \mathrm{mS\,cm^{-1}}$ can be achieved. For $Sb_{0.5}$ and $P_{0.5}$, ionic conductivities of $(4.88\pm0.673)\ \mathrm{mS\,cm^{-1}}$ and $(1.91\pm0.016)\ \mathrm{mS\,cm^{-1}}$ were determined. The phosphorus-rich ($P_{0.75}$) and antimony-rich ($Sb_{0.75}$) materials showed low ionic conductivities of $(0.043\pm0.004)\ \mathrm{mS\,cm^{-1}}$ and $(0.760\pm0.071)\ \mathrm{mS\,cm^{-1}}$. Corresponding activation energies (E_A) were calculated from Arrhenius fitting of the temperature-dependent conductivity (Figure 3a), with the values ranging from (0.19 ± 0.006) eV for EQ (lowest E_A) to (0.37 ± 0.002) eV for $P_{0.75}$ (highest E_A). As evident, lower activation energies were found for the highly conducting samples.

To characterize the transport properties in more detail, ^{7}Li PFG NMR spectroscopy measurements were performed in the temperature range of 30–70 °C. For EQ, $P_{0.75}$, $Sb_{0.5}$, and $Sb_{0.75}$, the spectra depicting echo intensity against gradient strength could be described with a one-component fit. In contrast, for $P_{0.5}$, $Si_{0.5}$, and $Ge_{0.5}$, two contributions were observed (apparent from plotting the natural logarithm of echo intensity against squared gradient strength). The experimental data were fitted with two contributions given by the Kärger equation for slowly exchanging phases (see Supporting Information for details).[36–38] In Figure S7 (Supporting Information), the echo intensity vs. gradient strength and the natural logarithm of echo intensity vs. squared gradient strength are exemplarily shown for $Sb_{0.75}$ and $Si_{0.5}$ to highlight the existence of a second diffusion component. Specifically, logarithmic plotting yields a straight line for a single diffusive motion while exhibiting a curvature if more than one component is present. This has been reported repeatedly for other lithium thiophosphates and is usually attributed to the presence of a secondary (amorphous) phase, which is unlikely here, though.[37,39] Regardless, the diffusion coefficient (D_{Li}) was determined to range from $(9.80\pm0.59)\cdot10^{-14}\ \mathrm{m^2\,s^{-1}}$ for $P_{0.75}$ to $(1.08\pm0.01)\cdot10^{-11}\ \mathrm{m^2\,s^{-1}}$ for $Si_{0.5}$ (major contribution). We note that for $P_{0.5}$, $Si_{0.5}$, and $Ge_{0.5}$, the D_{Li} of the minor contribution was on the order of $10^{-12}\ \mathrm{m^2\,s^{-1}}$.

Arrhenius fitting of the temperature-dependent lithium diffusion coefficients is shown in Figure 3b for all samples. This allowed determining the E_A, which was found to vary from (0.16 ± 0.003) eV for $Sb_{0.5}$ to (0.37 ± 0.014) eV for $P_{0.75}$, in good agreement with the EIS results. As mentioned above, in the case of $P_{0.5}$, $Si_{0.5}$, and $Ge_{0.5}$, a second
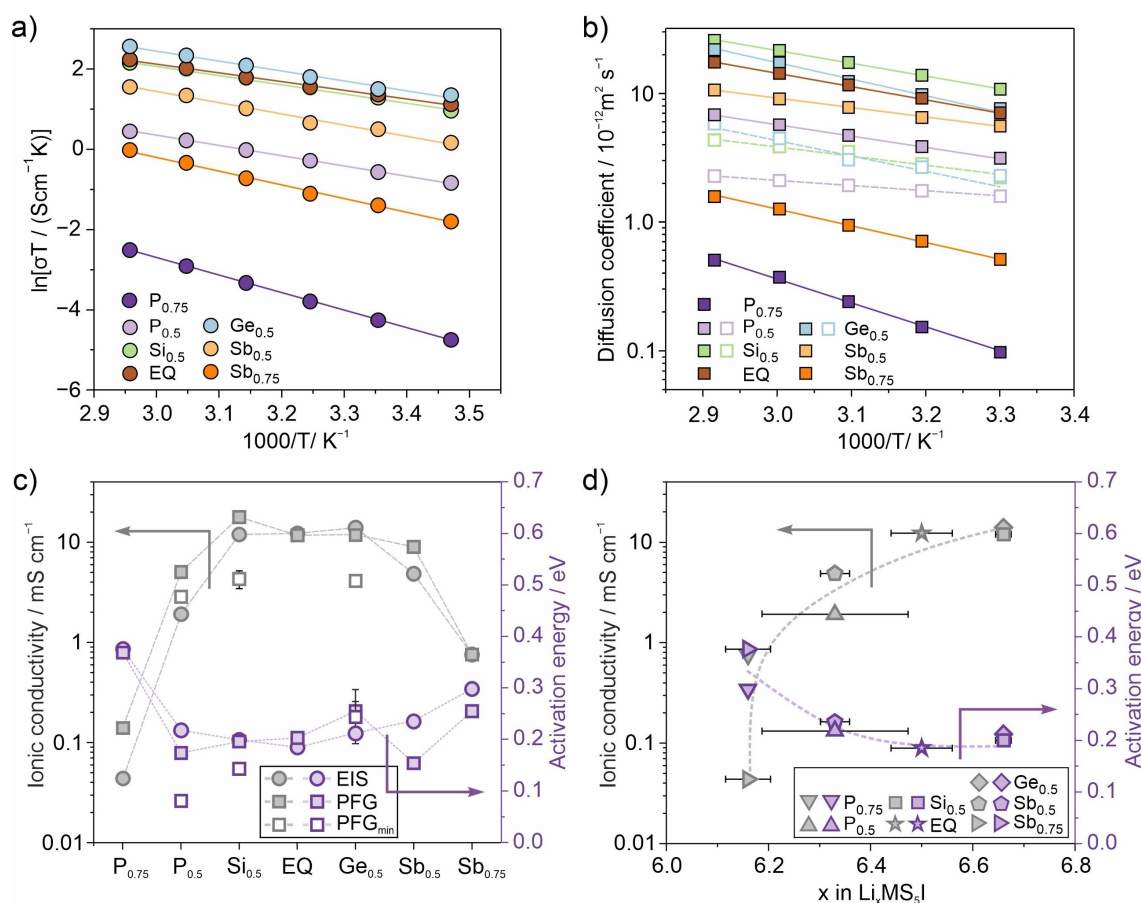

Figure 3. Charge-transport properties of the multication-substituted argyrodite SEs. Arrhenius plots of (a) temperature-dependent conductivities from EIS and (b) lithium diffusion coefficients determined by ^{7}Li PFG NMR spectroscopy. (c) Comparison of room-temperature ionic conductivities (gray) and activation energies (purple) from EIS (circles) and ^{7}Li PFG NMR spectroscopy (squares). (d) Relationship between refined Li content per formula unit and ionic conductivity and activation energy from EIS. The data for EQ was taken from the literature.[15,21] If no error bars are visible, the standard deviation is smaller than the symbol.

contribution had to be taken into account during fitting of the ^{7}Li PFG NMR data. Their activation energies are given in Table S16 (Supporting Information). Using the Nernst-Einstein equation, the ionic conductivities were calculated from the D_{Li}. Both the activation energies and ionic conductivities determined by EIS and ^{7}Li PFG NMR spectroscopy are shown in Figure 3c. As can be seen, they follow a similar trend for the different samples. In the case of $P_{0.5}$, $Si_{0.5}$, EQ, $Ge_{0.5}$, and $Sb_{0.5}$, room-temperature ionic conductivities above $1\,mS\,cm^{-1}$ were found. Notably, the ionic conductivity was above $10\,mS\,cm^{-1}$ for $Si_{0.5}$, $Ge_{0.5}$, and EQ (Table S16, Supporting Information), with the highest bulk conductivity of $17.94\,mS\,cm^{-1}$ from ^{7}Li PFG NMR spectroscopy for $Si_{0.5}$. Interestingly, the best-conducting samples did not show the lowest E_A. For $Si_{0.5}$, $Ge_{0.5}$, and EQ, activation energies of $(0.20 \pm 0.002)\,eV$, $(0.25 \pm 0.018)\,eV$, and $(0.20 \pm 0.002)\,eV$, respectively, were determined. As discussed previously, in the case of $P_{0.5}$, $Si_{0.5}$, and $Ge_{0.5}$, a second (minor) contribution had to be included to accurately describe the data. Their activation energies and ionic conductivities were lower than those of the major contributions.

Long-range lithium diffusion in argyrodites depends on the intercage jumps and, in particular, on the jump distance and frequency.[4] The Li substructure can be altered by occupying additional T2 and T4 positions, eventually leading to faster T5-T2-T2-T5 and T5-T4-T5 intercage jumps compared to T5-T5 (Figure 1f,g). This in turn may positively impact the D_{Li} and further give rise to two different diffusion components, as seen in the ^{7}Li PFG NMR data. However, some minor contribution from impurity phases cannot be fully excluded, although no signs were found in the diffraction experiments and from the MAS NMR spectroscopy measurements. Nevertheless, EIS and ^{7}Li PFG NMR spectroscopy revealed very high ionic conductivities for some of the samples, particularly for $Si_{0.5}$, $Ge_{0.5}$, and EQ, despite having very different cationic compositions. In the present study, alio- and isovalent substitutions on the phosphorus site were performed successfully, thus the Li content varied to some degree. To assess a possible correlation between Li concentration and charge-transport properties, Figure 3d illustrates the room-temperature ionic conductivity and activation energy as a function of Li content in the multication-substituted argyrodite SEs. At first glance, increased Li content leads to increased ionic conductivity and decreased activation energy. This strategy of "Li-stuffed" ion conductors has been practiced for a long time in the field of garnet-type SEs, but is scarcely discussed for lithium argyrodites.[41] As a matter of fact, it is important to note that the trend of increasing conductivity with increasing Li concentration is valid for most, if not all, highly conducting argyrodite-type solid solutions (e.g. $Li_{6+x}P_{1-x}Ge_xS_5I$ and $Li_{6+x}Sb_{1-x}Si_xS_5I$).[7,29] Higher Li contents typically lead to the appearance of hitherto unoccupied Li sites, accompanied by a decrease in activation energy. A similar trend is apparent for the samples employed here. In particular, the ionic conductivity strongly increased with increasing Li content, from 6.17 mol ($P_{0.75}$ and $Sb_{0.75}$) to 6.33 mol ($P_{0.5}$ and $Sb_{0.5}$) per formula unit. As can be seen

from Figure 3d, the ionic conductivity increased further upon increasing the Li content to 6.5 mol (EQ) and then leveled off at 6.66 mol ($Si_{0.5}$ and $Ge_{0.5}$). The activation energy decreased from 0.37 to ~0.20 eV with increasing Li content (up to 6.33 mol) and remained fairly constant for the other samples. However, the ionic conductivity differed significantly among them. Usually, low activation energies and increased ionic conductivity are associated with increased S^{2-}/X^- site inversion and occupation of additional ("intermediate") Li positions in argyrodite SEs. However, this kind of correlation is not valid for the multication-substituted lithium argyrodites discussed here. Nevertheless, it should be noted that the electronic conductivity determined by DC polarization measurements was found to be two to three orders of magnitude higher compared to that of other lithium thiophosphates reported in the literature (Table S17, Supporting Information).[12,42,43]

Taken together, the above analysis did not yield a clear correlation between the structural characteristics and the charge-transport properties. In particular, the observation of very low activation energies (except for $P_{0.75}$ and $Sb_{0.75}$) suggests that occupational disorder (configurational entropy) plays a non-negligible role in these materials. In the present series of lithium argyrodites with the general formula $Li_{6+x}MS_5I$ (M=P, Si, Ge, and Sb), the configurational entropy ΔS_{conf} can be deconvoluted into two contributions (Equations 1 and 2). The first involves $\Delta S_{conf,cation}$, i.e. cation mixing (Wyckoff position 4b), and the second $\Delta S_{conf,anion}$, i.e. anion mixing (Wyckoff positions 4a and 4d), according to:

$$\Delta S_{conf} = \Delta S_{conf,cation} + \Delta S_{conf,anion} \qquad (1)$$

and

$$\Delta S_{conf} = -R\left[\left(\sum_{i=1}^{N} x_i \ln x_i\right) + \left(\sum_{k=1}^{N} x_k \ln x_k\right)\right], \qquad (2)$$

with x_i and x_k representing the molar fraction of the cation and anion species occupying the 4b site and the 4a and 4d sites, respectively. R and N are the universal gas constant and the number of anions/cations, respectively. In general, the more equally the different species are distributed over the available sites, the higher ΔS_{conf} is, as schematically shown in Figure 4a for the cationic substituents. Overall, this means that the $\Delta S_{conf,cation}$ contribution is greatest when the $[PS_4]^{3-}$, $[SiS_4]^{4-}$, $[GeS_4]^{4-}$, and $[SbS_4]^{3-}$ tetrahedral units are equally distributed across the unit cell, leading to severe (local) structural distortions. Figure 4b shows the calculated ΔS_{conf} for the cation and anion disorder in the different samples. Interestingly, EQ having the highest cation disorder also exhibited the highest anion disorder, leading to $\Delta S_{conf} = -2.08R$. Since there was no apparent connection between the typical structural characteristics of lithium argyrodites and the transport properties, configurational entropy is assumed to play a prominent role. The correlation between ΔS_{conf} and activation energy and ionic conductivity from both EIS and ^{7}Li PFG NMR spectroscopy is depicted
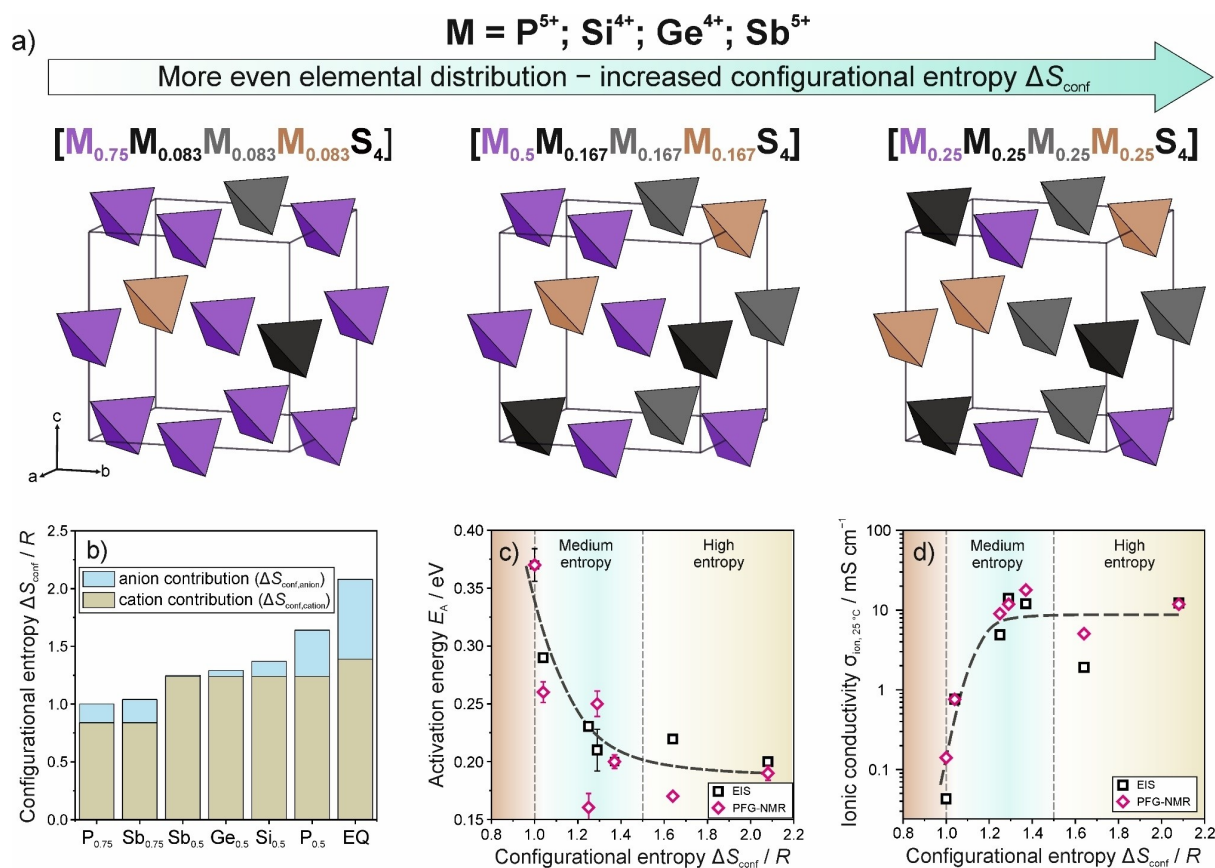
Figure 4. Configurational entropy-property relationships related to lithium diffusion. (a) Schematic representation of the tetrahedra arrangements in the unit cell showing that a more equal distribution leads to increased configurational entropy. (b) Configurational entropy contributions from cation and anion disorder. Correlation between configurational entropy and (c) activation energy and (d) ionic conductivity determined by EIS and ^{7}Li PFG NMR spectroscopy.

in Figure 4c and d, respectively, with the medium- and high-entropy regions being highlighted. As evident from the data, the activation energy decreases with increasing ΔS_{conf}, while the ionic conductivity increases. An increased ΔS_{conf} comes along with an increased vibrational entropy (ΔS_{vib}), which affects the lattice dynamics and distortion. Although it is challenging to unravel the effects of both contributions on mobility, one can assume that ΔS_{vib} positively affects the ion migration via phonon-mediated transport, ultimately leading to a lower energy barrier for diffusion.[23,44–47] In addition, the local structural distortions expressed by ΔS_{conf} lead to atomic displacement disorder, fostering overlapping Li-site energies (broadening) and facilitating long-range diffusion.[20] It should also be noted that aliovalent substitution probably leads to localized defect formation in the Li sublattice, which however has not been considered yet.

In general, ionic conductivity (Equation 3) can be expressed as the product of ion mobility (μ), charge (q), and charge-carrier density (n) according to:[48]

$$\sigma = nq\mu. \tag{3}$$

Because lithium is considered the only mobile charge carrier in the present series of samples, the conductivity solely depends upon the ion mobility and charge-carrier density. Although we have shown that there is a connection between the Li content per formula unit and the conductivity (Figure 3d), no such correlation is apparent with charge-carrier density. The ion mobility can be obtained from the diffusion coefficient (Equation 4), with q being the charge, and k_B and T representing the Boltzmann constant and temperature, respectively.

$$\mu = \frac{qD_{Li}}{k_B T} \tag{4}$$

In general, the diffusion coefficient is a measure of how quickly species (ions) move through the material due to random thermal motion and quantifies the rate at which they are diffusing. The correlation of ionic conductivity with occupational disorder derived from the cation sublattice demonstrates that increasing compositional complexity promotes the Li$^+$ mobility (Figure S8, Supporting Information). A comparison of lithium mobilities and densities for different argyrodites and LGPS is presented in Figure 5, and individual values are given in Table S18 (Supporting Information).[9] Interestingly, the multication-substituted argyrodite SEs exhibit Li$^+$ mobilities of $\mu > 10^{-6}$ cm^2 V^{-1} s^{-1},
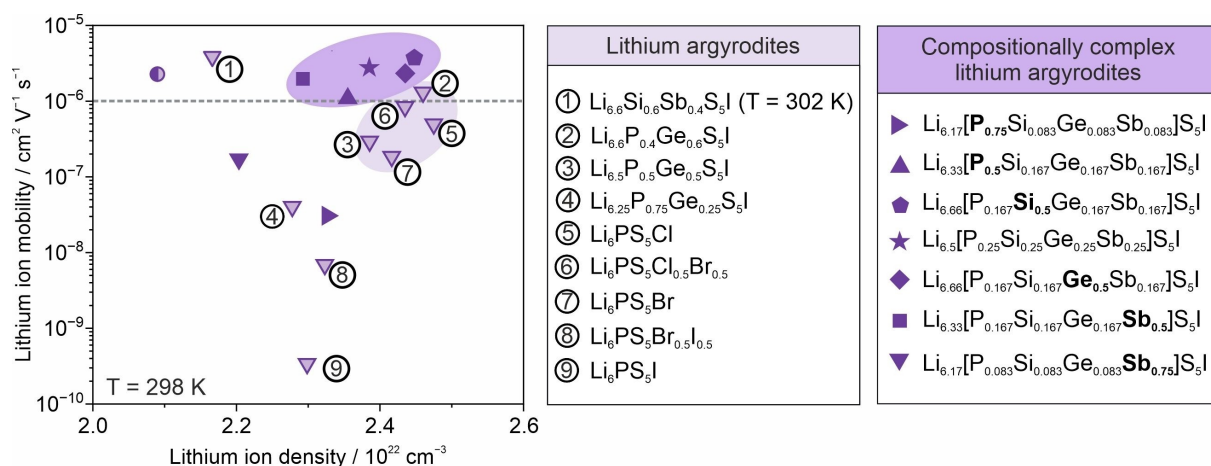
Figure 5. Li$^+$ mobility versus Li-ion density for different lithium argyrodites and Li$_{10}$GeP$_2$S$_{12}$ (denoted by the half-filled circle).[6–8,49,50]

one order of magnitude higher compared to other, more common highly conducting lithium argyrodites. Even the materials having a relatively low ionic conductivity such as P$_{0.5}$ [(1.91 ± 0.016) mS cm^{-1}] showed high ion mobilities (1.09·10^{-6} cm^2 V^{-1} s^{-1}), similar to that of LGPS (2.27·10^{-6} cm^2 V^{-1} s^{-1}, ~7 mS cm^{-1} at room temperature).[49] These results further emphasize that configurational entropy has a beneficial effect on lithium diffusivity.

Conclusions

In summary, we have investigated a series of multication-substituted lithium argyrodites with the general formula Li$_{6+x}$[M1$_a$M2$_b$M3$_c$M4$_d$]S$_5$I. All samples were subjected to thorough analysis of the crystal structure and charge-transport properties using a combination of powder diffraction techniques, ^{31}P, ^{29}Si, and ^{6}Li MAS NMR spectroscopy, EIS, and complementary ^{7}Li PFG NMR spectroscopy. We demonstrate that increasing configurational entropy, induced primarily by introducing cation disorder, correlates with decreasing activation energy and increasing ionic conductivity. This translates into room-temperature ionic conductivities above 10 mS cm^{-1} for some of the materials, with the highest of 17.9 mS cm^{-1} obtained for Li$_{6.66}$[P$_{0.167}$Si$_{0.5}$Ge$_{0.167}$Sb$_{0.167}$]S$_5$I. Tailoring the configurational entropy by altering the composition, we present—to the best of our knowledge—the first experimental evidence of a direct correlation between occupational disorder in the cationic host lattice and ion mobility. Overall, the data point toward the possibility of enhancing conductivity in ceramic ion conductors via entropy engineering, potentially also allowing to improve the (electro)chemical stability and mechanical properties.

Conflict of Interest

The authors declare the following competing interest(s): A patent was filed for this work through BASF SE and Karlsruher Institut für Technologie (KIT).

Data Availability Statement

The data that support the findings of this study are available from the corresponding author upon reasonable request.

[1] J. Janek, W. G. Zeier, *Nat. Energy* **2023**, *8*, 230–240.

[2] A. Manthiram, X. Yu, S. Wang, *Nat. Rev. Mater.* **2017**, *2*, 1–16.

[3] Z. Zhang, Y. Shao, B. Lotsch, Y. S. Hu, H. Li, J. Janek, L. F. Nazar, C. W. Nan, J. Maier, M. Armand, L. Chen, *Energy Environ. Sci.* **2018**, *11*, 1945–1976.

[4] L. Zhou, N. Minafra, W. G. Zeier, L. F. Nazar, *Acc. Chem. Res.* **2021**, *54*, 2717–2728.

[5] H. J. Deiseroth, S. T. Kong, H. Eckert, J. Vannahme, C. Reiner, T. Zaiß, M. Schlosser, *Angew. Chem. Int. Ed.* **2008**, *47*, 755–758.

[6] M. A. Kraft, S. P. Culver, M. Calderon, F. Böcher, T. Krauskopf, A. Senyshyn, C. Dietrich, A. Zevalkink, J. Janek, W. G. Zeier, *J. Am. Chem. Soc.* **2017**, *139*, 10909–10918.

[7] L. Zhou, A. Assoud, Q. Zhang, X. Wu, L. F. Nazar, *J. Am. Chem. Soc.* **2019**, *141*, 19002–19013.

[8] M. A. Kraft, S. Ohno, T. Zinkevich, R. Koerver, S. P. Culver, T. Fuchs, A. Senyshyn, S. Indris, B. J. Morgan, W. G. Zeier, *J. Am. Chem. Soc.* **2018**, *140*, 16330–16339.

[9] J. C. Bachman, S. Muy, A. Grimaud, H. H. Chang, N. Pour, S. F. Lux, O. Paschos, F. Maglia, S. Lupart, P. Lamp, L. Giordano, Y. Shao-Horn, *Chem. Rev.* **2016**, *116*, 140–162.

[10] T. Famprikis, P. Canepa, J. A. Dawson, M. S. Islam, C. Masquelier, *Nat. Mater.* **2019**, *18*, 1278–1291.

[11] Y. Wang, W. D. Richards, S. P. Ong, L. J. Miara, J. C. Kim, Y. Mo, G. Ceder, *Nat. Mater.* **2015**, *14*, 1026–1031.

[12] P. Adeli, J. D. Bazak, K. H. Park, I. Kochetkov, A. Huq, G. R. Goward, L. F. Nazar, *Angew. Chem.* **2019**, *131*, 8773–8778.

[13] J. Xu, *Mater. Futures* **2023**, *2*, 047501.

[14] F. Strauss, J. Lin, M. Duffiet, K. Wang, T. Zinkevich, A.-L. Hansen, S. Indris, T. Brezesinski, *ACS Materials Lett.* **2022**, *4*, 418–423.

[15] J. Lin, G. Cherkashinin, M. Schäfer, G. Melinte, S. Indris, A. Kondrakov, J. Janek, T. Brezesinski, F. Strauss, *ACS Materials Lett.* **2022**, *4*, 2187–2194.

[16] Y. Li, S. Song, H. Kim, K. Nomoto, H. Kim, X. Sun, S. Hori, K. Suzuki, N. Matsui, M. Hirayama, T. Mizoguchi, T. Saito, T. Kamiyama, R. Kanno, *Science* **2023**, *381*, 50–53.

[17] Y. Ma, Y. Ma, Q. Wang, S. Schweidler, M. Botros, T. Fu, H. Hahn, T. Brezesinski, B. Breitung, *Energy Environ. Sci.* **2021**, *14*, 2883–2905.

[18] P. Wang, S. Patel, H. Liu, P. H. Chien, X. Feng, L. Gao, B. Chen, J. Liu, Y. Y. Hu, *Adv. Funct. Mater.* **2023**, *33*, 1–11.

[19] S. K. Jung, H. Gwon, H. Kim, G. Yoon, D. Shin, J. Hong, C. Jung, J. S. Kim, *Nat. Commun.* **2022**, *13*, 7638.

[20] Y. Zeng, B. Ouyang, J. Liu, Y. W. Byeon, Z. Cai, L. J. Miara, Y. Wang, G. Ceder, *Science* **2022**, *378*, 1320–1324.

[21] J. Lin, M. Schaller, G. Cherkashinin, S. Indris, J. Du, C. Ritter, A. Kondrakov, J. Janek, T. Brezesinski, F. Strauss, *Small* **2024**, *20*, 2306832.

[22] F. Strauss, J. Lin, A. Kondrakov, T. Brezesinski, *Matter* **2023**, *6*, 1068–1070.

[23] S. Li, J. Lin, M. Schaller, S. Indris, X. Zhang, T. Brezesinski, C.-W. Nan, S. Wang, F. Strauss, *Angew. Chem. Int. Ed.* **2023**, *62*, e202314155.

[24] Q. Wang, Y. Zhou, X. Wang, H. Guo, S. Gong, Z. Yao, F. Wu, J. Wang, S. Ganapathy, X. Bai, B. Li, C. Zhao, J. Janek, M. Wagemaker, *Nat. Commun.* **2024**, *15*, 1050.

[25] Z. Song, T. Wang, H. Yang, W. H. Kan, Y. Chen, Q. Yu, L. Wang, Y. Zhang, Y. Dai, H. Chen, W. Yin, T. Honda, M. Avdeev, H. Xu, J. Ma, Y. Huang, W. Luo, *Nat. Commun.* **2024**, *15*, 1481.

[26] W. Li, Z. Chen, Y. Chen, L. Zhang, G. Liu, L. Yao, *Adv. Funct. Mater.* **2024**, *1–9*, 2312832.

[27] R. D. Shannon, *Acta Crystallogr.* **1976**, *A*, 751–767.

[28] S. Ohno, B. Helm, T. Fuchs, G. Dewald, M. A. Kraft, S. P. Culver, A. Senyshyn, W. G. Zeier, *Chem. Mater.* **2019**, *31*, 4936–4944.

[29] K. Hogrefe, N. Minafra, I. Hanghofer, A. Banik, W. G. Zeier, H. M. R. Wilkening, *J. Am. Chem. Soc.* **2022**, *144*, 1795–1812.

[30] N. Minafra, M. A. Kraft, T. Bernges, C. Li, R. Schlem, B. J. Morgan, W. G. Zeier, S. P. Culver, T. Krauskopf, A. Senyshyn, W. G. Zeier, *Inorg. Chem.* **2020**, *59*, 11009–11019.

[31] R. Schlenker, A. L. Hansen, A. Senyshyn, T. Zinkevich, M. Knapp, T. Hupfer, H. Ehrenberg, S. Indris, *Chem. Mater.* **2020**, *32*, 8420–8430.

[32] I. Hanghofer, M. Brinek, S. L. Eisbacher, B. Bitschnau, M. Volck, V. Hennige, I. Hanzu, D. Rettenwander, H. M. R. Wilkening, *Phys. Chem. Chem. Phys.* **2019**, *21*, 8489–8507.

[33] M. Kaus, H. Stöffler, M. Yavuz, T. Zinkevich, M. Knapp, H. Ehrenberg, S. Indris, *J. Phys. Chem. C* **2017**, *121*, 23370–23376.

[34] F. Hartmann, A. Benkada, S. Indris, M. Poschmann, H. Lühmann, P. Duchstein, D. Zahn, W. Bensch, *Angew. Chem. Int. Ed.* **2022**, *61*, 1–10.

[35] S. Harm, A. K. Hatz, I. Moudrakovski, R. Eger, A. Kuhn, C. Hoch, B. V. Lotsch, *Chem. Mater.* **2019**, *31*, 1280–1288.

[36] D. Wijesekera, T. Stait-Gardner, A. Gupta, J. Chen, G. Zheng, A. M. Torres, W. S. Price, *Concepts Magn. Reson. Part A* **2018**, *47A*, 1–12.

[37] E. P. Ramos, J. D. Bazak, A. Assoud, A. Huq, G. Goward, L. F. Nazar, *ACS Appl. Mater. Interfaces* **2022**, *14*, 56767–56779.

[38] W. S. Price, *Concepts Magn. Reson.* **1998**, *10*, 197–237.

[39] R. Calaminus, S. Harm, D. H. Fabini, L. G. Balzat, A. K. Hatz, V. Duppel, I. Moudrakovski, B. V. Lotsch, *Chem. Mater.* **2022**, *34*, 7666–7677.

[40] P.-H. Chien, B. Ouyang, X. Feng, L. Dong, D. Mitlin, J. Nanda, J. Liu, *Chem. Mater.* **2024**, *36*(1), 382–393.

[41] W. G. Zeier, *Dalton Trans.* **2014**, *43*, 16133–16138.

[42] F. Strauss, J. Lin, L. Karger, D. Weber, T. Brezesinski, *Inorg. Chem.* **2022**, *61*, 5885–5890.

[43] S. J. Sedlmaier, S. Indris, C. Dietrich, M. Yavuz, C. Dräger, F. Von Seggern, H. Sommer, J. Janek, *Chem. Mater.* **2017**, *29*, 1830–1835.

[44] J. Ding, PhD thesis, Duke University **2022**, 1–227.

[45] S. Muy, R. Schlem, Y. Shao-Horn, W. G. Zeier, *Adv. Energy Mater.* **2021**, *11*, 2002787.

[46] S. Muy, J. C. Bachman, L. Giordano, H. H. Chang, D. L. Abernathy, D. Bansal, O. Delaire, S. Hori, R. Kanno, F. Maglia, S. Lupart, P. Lamp, Y. Shao-Horn, *Energy Environ. Sci.* **2018**, *11*, 850–859.

[47] B. Ahammed, E. Ertekin, *Adv. Mater.* **2024**, *6*, 1–15.

[48] M. Sotoudeh, S. Baumgart, M. Dillenz, J. Döhn, K. Forster-Tonigold, K. Helmbrecht, D. Stottmeister, A. Groß, *Adv. Energy Mater.* **2023**, *14*, 2302550.

[49] T. Krauskopf, S. P. Culver, W. G. Zeier, *Chem. Mater.* **2018**, *30*, 1791–1798.

[50] N. Minafra, S. P. Culver, T. Krauskopf, A. Senyshyn, W. G. Zeier, *J. Mater. Chem. A* **2018**, *6*, 645–651.